W-shaped permeability evolution of coal with supercritical CO_2 phase transition

Sheng Zhi[a,*], Derek Elsworth[a], Liyuan Liu[b]

[a] Department of Energy and Mineral Engineering, EMS Energy Institute and G3 Center, Pennsylvania State University, University Park, PA 16802, USA
[b] School of Civil and Resource Engineering, University of Science & Technology Beijing, Beijing, China

A B S T R A C T

Gaseous CO_2 becomes a supercritical liquid when temperature and pressure transit the critical point (31.1 °C and 7.4 MPa) – a typical state for CO_2 storage for carbon sequestration and CO_2 injection in enhanced coalbed methane/shale recovery. Therefore, it is essential to define the evolution of coal permeability inclusive of this phase transition. This study presents experimental measurements of coal permeability across the CO_2/$SCCO_2$ transition over typical ranges of confining stress (3–15 MPa) and pore pressures (1–13 MPa) at a constant temperature of 40 °C. The results show that contrary to the typical U-shaped permeability -vs- pressure evolution in the subcritical region, a second permeability minimum occurs in the vicinity of the critical pressure – even after the impacts of viscosity transition are accommodated. Permeability to $SCCO_2$ is almost two-orders-of-magnitude smaller than its initial permeability to subcritical-CO_2. The phase transition from sub-critical to supercritical state controls the W-shaped coal permeability profile. Permeability in the same coal is indexed relative to non-sorbing Helium (He) and slightly-adsorbing Nitrogen (N_2) to probe the origins of the W-shaped permeability profile around the $SCCO_2$ phase transition. Observed irreversible changes in mechanical properties driven by the $SCCO_2$ phase transition are linked to the observed permeability reduction. First, observed reductions in coal strength and stiffness after $SCCO_2$ saturation indicate a significant weakening effect - $SCCO_2$ acts as a strong plasticizer enabling rearrangement of the physical structure and adding molecular mobility. The softened coal responds to increased compressional deformation and cleat closure under the same effective stress, resulting in a net permeability reduction in the supercritical region countering any influences of permeability-enhancing microcrack formation. Second, the $SCCO_2$ permeability is further reduced by a large increase in sorption-induced swelling observed after the transition. Measured swelling strains indicate a > 90% increase in $SCCO_2$ sorption-induced swelling relative to Langmuir response at 13 MPa. The enlarged $SCCO_2$ adsorption capacity presumably results from the slightly polar nature of the $SCCO_2$ dimer and the increased $SCCO_2$ density. Permeability reduction due to plasticization and increased swelling is shown to dominate over permeability increases driven by brittle damage.

1. Introduction

The study of interactions between coal and CO_2 is an essential issue for CO_2 applications in the energy industry. To reduce greenhouse gas emission, long-term storage of carbon dioxide (CO_2) in deep unmineable coal seams is proposed as a promising potential method for CO_2 sequestration (Lal, 2008). As a sorbing gas, CO_2 not only exists inside fractures as a free gas but is also adsorbed into coal matrix as an adsorbed phase. The strong CO_2 adsorption affinity and the large surface area provided by the porous structure in the coal matrix make CO_2 sequestration in coal seams as a viable option. For methane-rich coal seams, the injected CO_2 tends to displace the already adsorbed methane and helps facilitate methane extraction, which has been implemented and tested as CO_2 enhanced coalbed methane (CO_2-ECBM) production (Van Bergen et al., 2005). During CO_2-ECBM, the desorption of CH_4 with injection of CO_2 into the coal matrix results from the higher attraction and stronger Van der Waals bonds between the coal mass and CO_2 compared to those for methane (Ranathunga et al., 2016; White

et al., 2005). Moreover, CO_2 is co-produced with methane by the anaerobic methanogens resulting from bio-gasification treatment in microbially-enhanced CBM reservoirs (Zhang et al., 2015; Zhi et al., 2018). The generated CO_2 must also be extracted from the production well during methane recovery. Among these applications involving CO_2 injection/production, coal permeability evolution is one of the most important properties controlling how CO_2 is stored and transported in coal seams.

Coal is typically characterized as a dual porosity-dual permeability system (G. Wang et al., 2018; Wu et al., 2010, 2011): the coal matrix system that comprises micro- and meso- pores, and a cleat/fracture system that consist of macro-pores and interconnected natural fractures (Gensterblum et al., 2014a; Liu et al., 2011). Coal permeability is controlled by the conductivity of both coal matrix and fracture systems. Due to the lower permeability in the matrix, the natural fractures are the principal pathway for gas transport during injection and production. However, gas diffusion processes through the coal matrix are important when flow in the fracture networks are impeded. When a

---

* Corresponding author.
  E-mail address: suz140@psu.edu (S. Zhi).

Fig. 1. Typical core sample used in this study.

sorbing gas, like CO_2, is present, coal swelling and shrinkage, due to gas sorption and desorption, significantly affects the permeability of the coal reservoir. Recent laboratory-scale experiments (Ranathunga et al., 2016; Robertson and Christiansen, 2007; Vishal, 2016; Wang et al., 2013) and field-scale projects (Fujioka et al., 2010; Mavor et al., 2004; Syed et al., 2013) have examined the influences of effective stress and sorption-induced strains on coal permeability. In general, these studies show that compared to non-sorbing gases, the matrix swelling induced by CO_2 adsorption results in fracture closure, porosity decrease, and consequently permeability reduction (Izadi et al., 2011; Wang et al., 2011). When pore pressure is intermediate, the CO_2 adsorption results in the minimum permeability. As pore pressure increases from this minimum permeability, the influence of reduced effective stress predominates and permeability increases. This is the typical U-shaped (or V-shaped) permeability profile for CO_2 and CH_4 adsorption that has been widely observed in laboratory experiments (Kumar et al., 2015; Robertson and Christiansen, 2007; Wang et al., 2011; Wang et al., 2015). Among these studies on CO_2 impacts, adsorption-induced permeability change has been examined only under gaseous and liquid state CO_2 (sub-critical) conditions.

Gaseous CO_2 becomes a supercritical liquid when temperature and pressure are at or above the critical point (31.1 °C and 7.3 MPa) – a characteristic readily achieved in ECBM or CO_2 sequestration. Beyond this critical point, the fluid properties of supercritical CO_2 change drastically, resulting in a liquid-like density and a gas-like viscosity (McBride-Wright et al., 2015). Many investigations have been conducted on the impacts of $SCCO_2$ on coal adsorption and mechanical characteristics, but the potential influence of $SCCO_2$ on coal permeability remains poorly understood. A > 40% reduction in uniaxial compressive strength (UCS) and > 100% reduction in elastic modulus have been observed following $SCCO_2$ saturation (Perera et al., 2013b). The significantly reduced UCS and elastic modulus indicate that $SCCO_2$ has a strong weakening and plasticizing effect on coal. This behavior may result from newly generated micro-cleats (micro-fracturing) in mineral phases resulting in porosity increasing from 1.2% to 5.6% (Massarotto et al., 2010; Zhang et al., 2016). After $SCCO_2$ saturation, a critically smaller permeability was observed at 10–20 MPa pore pressure range compared to N_2, owing to the higher affinity of $SCCO_2$ to coal matrix (Vishal, 2016). This assumption was confirmed by the $SCCO_2$ adsorption measurement. As the pore pressure increases, a measurable increase in the adsorbed CO_2 amount occurred after the

vicinity of the critical point (Toribio et al., 2005). The $SCCO_2$ permeability reduction can be further enlarged by increasing the coal rank because of the larger carbon content in high-ranked coal (Ranathunga et al., 2016). An around 10-fold decrease in $SCCO_2$ permeability was measured when comparing coal permeability to subcritical and supercritical CO_2 permeability for the same sample (Perera et al., 2011a). However, the measured pressure range is discontinuous in the two phases, without the critical range of 5–7.5 MPa.

None of these prior studies have provided the entire CO_2 permeability profile spanning subcritical to supercritical states. A significant gap remains of how coal permeability responds as pore pressure transits from low to high and above the critical temperature. The lack of such a permeability profile also limits permeability modeling to the sub-critical range and the fitting of the typical U-shaped permeability model (Liu et al., 2017; Peng et al., 2017; Zhang et al., 2018). This work explores coal permeability evolution for the full range of pressures transiting CO_2/$SCCO_2$ inclusive of the phase transition.

2. Experimental methodology

We measure the evolution of permeability and strength on samples of volatile bituminous coals from the Illinois basin. Recreated in situ temperatures and pressures are used with low permeabilities requiring the use of pulse-decay permeability measurements. The sample preparation and experimental techniques are introduced in the following.

2.1. Sample preparation

The bituminous coals used in this study were collected from a depth of ~200 m in southwest Illinois. Cylindrical samples with a diameter of 1 in. (25.4 mm) were cored from the coal blocks perpendicular to bedding, using a low-speed core bit. Each specimen was then trimmed by circular saw to a length of 2 in. (50.8 mm). The top and bottom surfaces of the cut samples were ground smooth and parallel for testing, using a face grinder. Fig. 1 shows a typical core sample containing natural cleats (white arrows) and imparting natural variability. These samples were used for both permeability and triaxial strength measurements.

The results of proximate analysis of the bituminous coal are summarized in Table 1. The weight percentages of fixed carbon and volatile matter were 41% and 37%, respectively. The calorific value of the

Table 1
Proximate analysis for Illinois coal.

Moisture	Fixed carbon	Volatile matter	Ash
3%	48%	42%	7%
Calorific value	25,121–26,284 kJ/kg		
Rank	High volatile bituminous		

sample was measured using powdered coal particles that passed through a #200 mesh sieve. The average matrix density of the coal under unconfined conditions was 1234 kg/m³.

2.2. Core holder apparatus

The high-pressure tri-axial configuration used for permeability and strength measurements is shown schematically in Fig. 2. The core sample is jacketed and confined in a steel core holder capable of applying confining and axial stresses to 35 MPa to a resolution of ± 0.1 kPa. Either distilled water or hydraulic oil are used as confining fluids with the sample and platens isolated from the hydraulic fluids by a high-strength polyvinyl chloride (PVC) rubber jacket. Permeability may be measured down to 10^{-23} m² by pulse or steady-state protocols. Axial displacement is measured externally using a linear variable displacement transducer (LVDT) in contact with the moving piston (resolution to 1 μm). The stiffness of the loading system is 85 kN/mm at zero confining stress. Axial strain of the sample is calculated from measured axial displacement corrected for the compliance of the loading system. Temperature is controlled by encasing the tri-axial core holder in a furnace with controlled temperature.

2.3. Experimental procedure

2.3.1. Permeability measurements

The sample with platens was installed inside the PVC rubber sheath and confined within the tri-axial coreholder. Axial and confining stresses were retained equivalent. Permeability was measured by pulse-decay. When sorptive fluids were present the core sample was encased in aluminum foil to prevent diffusion through the rubber sheath. Individual pore pressures were maintained for 6 h or 48 h for the different gases to allow complete equilibrium before measuring permeability.

Two series of permeability experiments were designed to simulate in-situ stress conditions. The effect of stratum depth is represented by varying confining stress with constant pore pressure. The effect of reservoir pressure on injectivity or productivity is represented by a varying pore pressure under a constant confining stress. For sample T1501-He and T1502-N$_2$, the axial and confining stresses were set to 15 MPa with pore pressure increased from 1 to 13 MPa in increments of 2 MPa. For sample T1503-CO$_2$ and T1504-CO$_2$ the permeability experiments were first conducted at a constant pore pressure of 1 MPa with confining stress increased from 3 to 15 MPa – resulting in variable effective stress at constant pore pressure. Following this, CO$_2$ permeability was then measured at pore pressures in the range 1–13 MPa at a constant confining stress of 15 MPa. A constant temperature of 40 °C was maintained in all experiments to enable the phase transition to occur for CO$_2$ at a pore pressure of ~7 MPa. The experimental configurations are summarized in Table 2.

The intrinsic permeability is measured by pulse decay at each incremented pore pressure with only a small pressure differential (100 kPa) applied between upstream and downstream reservoirs - to retain effective stress near constant throughout the sample. Supercritical CO$_2$ is considered as a Darcy's flow since it has gas-like compressibility. Assuming isothermal conditions and that the ideal gas law applies, permeability is evaluated as (Wang et al., 2015)

$$k = \frac{\alpha \mu C_g L}{f A \left(\frac{1}{V_u} + \frac{1}{V_d} \right)}$$

(1)

where α is the slope of pressure decay versus time in a semi-log plot, represented as $\log \frac{d\left(\frac{p_u - p_d}{p_{u0} - p_{d0}}\right)}{dt}$. μ and C$_g$ are the gas viscosity and compressibility, respectively. L is the length and A is the cross-sectional area of the sample. V$_u$ and V$_d$ are the volumes of upstream and downstream reservoirs, respectively. The factor f reduces to 1.0 as V$_u$ and V$_d$ are much greater than the pore volume inside the sample (Jones, 1997). It is worth noting that for a sorptive gas, the measured permeability is a result of both the Klinkenberg slippage and sorption-induced swelling/shrinkage effect, especially at low effective stresses (< 5 MPa). Since there are only gas and gas-like fluids tested in this study, the intrinsic permeability is adopted from the experimental measurements.

2.3.2. Triaxial strength measurements

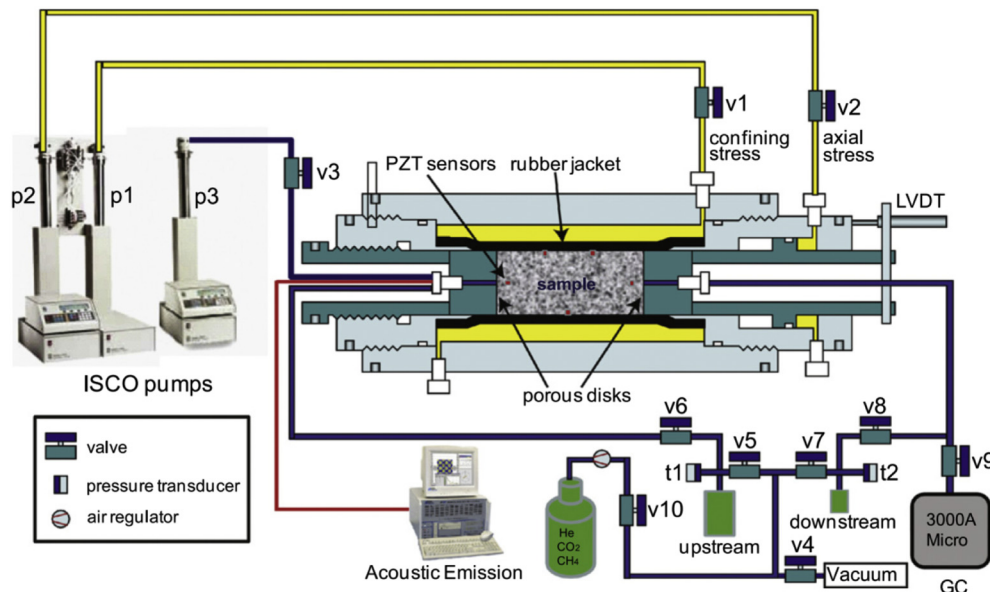Following the measurement of permeability, the confining and axial

Fig. 2. Schematic of the experimental apparatus used in this study (Wang et al., 2011).

Table 2
Summary of experiment configurations and saturation phases for the testing.

Sample no.	Saturation phase	Confining stress (MPa)	Axial stress (MPa)	Pore pressure (MPa)	T (°C)
T1501-He	Gaseous	15	15	1,3,5,7,9,11,13	40
T1502-N_2	Gaseous	15	15	1,3,5,7,9,11,13	40
T1503-CO_2 (6 h)	Gaseous	3,5,7,9,11,13,15	3,5,7,9,11,13,15	1	
	Gaseous	15	15	1,3,5,7	40
	Supercritical	15	15	7.5, 8, 9, 11, 13	
T1504-CO_2 (48 h)	Gaseous	3,5,7,9,11,13,15	3,5,7,9,11,13,15	1	
	Gaseous	15	15	1,3,5,7	40
	Supercritical	15	15	7.5,8,8.5,9,11,13	

Note: Experiments were conducted at constant confining (axial) stress for T1501&1502. Experiments were conducted at either constant pore pressure or constant confining (axial) stress for T1503&1504.

stresses and pore pressures were slowly decreased at the same rate to minimize any mechanical damage to the physical structure of the coal samples. At a confining stress (same as axial stress) of 1.5 MPa and pore pressure of 1.0 MPa the sample was axially loaded to failure and deformations were recorded at 10 Hz.

3. Experimental results

We measure permeability and strength for the four samples under N_2, He and CO_2 saturation to define the role of the transition of CO_2 from sub- to super-critical in driving structural changes in the coal.

3.1. W-shaped permeability evolution

The permeability data of Fig. 3 are measured after 6-h and 48-h saturation for specimens T1503-CO_2 and T1504-CO_2, respectively. CO_2 pressure is increased from 1 to 13 MPa at 40 °C and its gaseous phase changes to supercritical phase at ~7.4 MPa – capturing the full permeability evolution with phase transition.

A W-shaped curve of permeability evolution with pressure is observed for both T1503 and T1504. In this W-shaped curve, the permeability profile decreases and then increases around the Langmuir pressure and then this behavior repeats around the supercritical pressure transition. As shown in Fig. 3(A), permeability is decreased by 50%, possibly due to sorption-induced swelling, as the pressure increases from 1 to 5 MPa. After this decrease, the permeability then slightly rises between 5 and 7 MPa. The rising trend initiates at 7 MPa and is indicated by the solid red curve in the numerical modeling of subcritical CO_2 permeability (Liu et al., 2011; Zhi and Elsworth, 2016). We explore the role of sorption-induced swelling in driving this change in super-critical permeabilty. As the sorption-induced volumetric strain ε_s is fit to a Langmuir isotherm curve, the change in sorption-induced volumetric strain with pore pressure variation can be written as

$$\Delta\varepsilon_s = \frac{\varepsilon_L P_L (P - P_0)}{(P_L + P_0)(P_L + P)} \tag{2}$$

where ε_L and P_L are the Langmuir strain constant and Langmuir pressure constant, respectively. P_0 is the initial pore pressure. The change in fracture porosity ϕ_f can be defined as (Liu et al., 2011)

$$\Delta\phi_f = -\frac{3\Delta\sigma_{eff}}{E}(1 - R_m) - f_s \Delta\varepsilon_s \tag{3}$$

where $\Delta\sigma_{eff}$ is the effective stress change induced by pore pressure variation. E and E_m are the bulk moduli of the coal mass and coal matrix, respectively. $R_m = E/E_m$ is introduced as the elastic modulus reduction ratio to depict the ratio of the partitioned strains for the coal matrix system. $R_m = 0$ represents an infinitely soft fracture and $R_m = 1$ an infinitely stiff fracture. The experimentally measured Langmuir constants are small relative to those reported elsewhere for bituminous coal – possibly since they are measured under stress-controlled confinement instead of under free-swelling conditions. However, the

sorption-induced strain is much larger than the measured bulk strain, especially at high effective stress. Therefore, a sorption amplification factor f_s is introduced to effectively replicate the subcritical CO_2 permeability results. f_s is determined by fitting the experimental permeability data with the measured bulk strain. Similarly, the matrix porosity change can be defined as $\Delta\phi_m = \frac{3\Delta\sigma_{eff}}{E}R_m$.

Using the cubic relationship between coal permeability and porosity yields (Seidle and Huitt, 1995)

$$k_f = \left(1 + \frac{\Delta\phi_f}{\phi_{f0}}\right)^3$$

$$k_m = \left(1 + \frac{\Delta\phi_m}{\phi_{m0}}\right)^3 \tag{4}$$

where k_f and k_m represent fracture and matrix permeability, respectively. The resultant coal permeability k can be written as (Van Golf-Racht, 1982)

$$k = k_f + k_m = \frac{k_{m0}}{k_{m0} + k_{f0}}\frac{k_m}{k_{m0}} + \frac{k_{f0}}{k_{m0} + k_{f0}}\frac{k_f}{k_{f0}} \tag{5}$$

All modeling parameters are listed in Table 3. The modeling result indicates that the permeability should continue to increase above 7 MPa as the effect of sorption-induced swelling is dominated by effective stress-controlled mechanical deformation. However, an observable permeability drop occurs at 7.5 MPa, immediately above the transition to supercritical state. For T1503-CO_2, a permeability reduction of ~53% occurs at a pressure of 7.5 MPa, and the minimum permeability is 2.07×10^{-17} m^2 at a pressure of 8 MPa. The $SCCO_2$ permeability rebounds after reaching its minimum as the effect of $SCCO_2$ adsorption-induced swelling is again surpassed by that of mechanical stress. When pore pressure increases to 13 MPa and confining stress is retained at 15 MPa, the $SCCO_2$ permeability is finally elevated to 212% of its initial permeability.

Similarly, in Fig. 3(B), coal permeability decreases by ~85% due to sorption-induced swelling as pressure increases from 1 to 5 MPa. After decreasing, permeability then rises slightly between 5 and 7 MPa. The rising trend occurs at 7 MPa and is shown as the red dashed curve of the numerical modeling of permeability. A fairly steep permeability drop occurs at 7.5 MPa, which is the first pressure point measured for CO_2 permeability in the supercritical state. Compared with T1503-CO_2, a much larger permeability reduction occurs in T1504-CO_2 at 9 MPa, reaching 4.44×10^{-20} m^2 and only ~1.4% of its initial permeability. The larger permeability reduction occurs to T1503-CO_2 because of its lower pristine permeability before the test. The narrow fractures and small pores are more sensitive to the decrease induced by the CO_2 sorption. The $SCCO_2$ permeability rebounds after reaching its minimum as the effect of $SCCO_2$ adsorption-induced swelling is again surpassed by mechanical stress. When pore pressure increases to 13 MPa and confining stress is retained at 15 MPa, and the $SCCO_2$ permeability is finally elevated to 48% of its initial permeability.
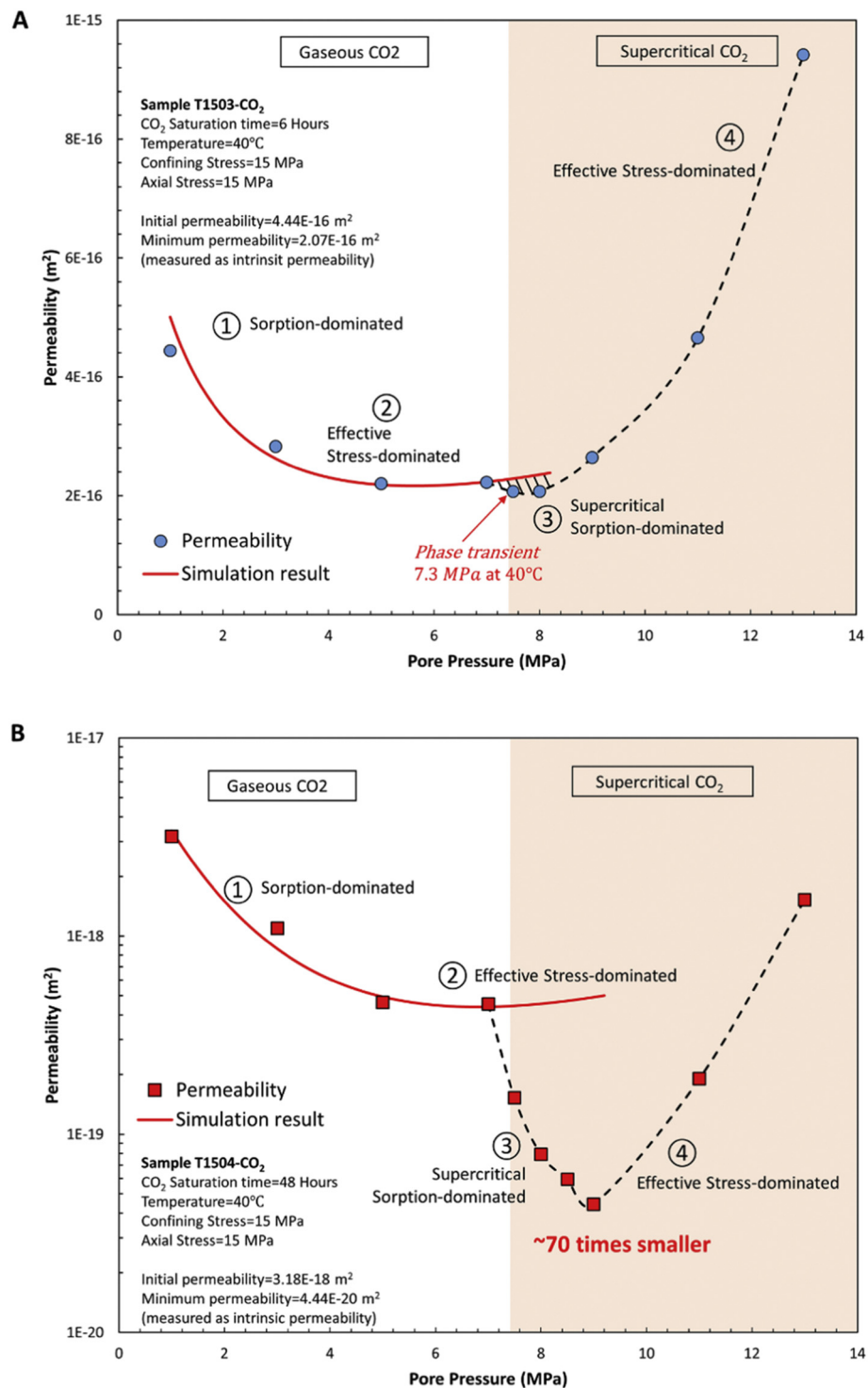
Fig. 3. Permeability evolution versus pore pressure in both subcritical and supercritical CO_2 regions. The blue circles and red squares represent the experimental measurements, and the red solid line represents the results of numerical modeling to fit the experimental data in the subcritical region. (A) Sample T1503-CO_2; (B) Sample T1504-CO_2. (For interpretation of the references to colour in this figure legend, the reader is referred to the web version of this article.)

3.2. Time-dependent CO_2 adsorption and coal permeability

Sample T1504-CO_2 was chosen to investigate the effect of saturation time on CO_2/$SCCO_2$ adsorption and permeability. The sample was subjected to subcritical CO_2 adsorption at saturation pressures of 1, 3, 5,7 MPa and supercritical CO_2 adsorption at saturation pressure of 7.5, 8, 8.5, 9, 11, 13 MPa. For each pore pressure, permeability measurements were initiated at 6 h and at subsequent increments of 6 h until reaching 48 h.

reaching 48 h.

Fig. 4 shows measured permeabilities with saturation time at each pore pressure for sample T1504-CO_2. It can be observed that for each pore pressure, permeability decreases as saturation time increases. The absolute permeability loss occurs principally at lower pressures and this loss decreases with increasing injection pressure. In addition, Fig. 5 summarizes the permeability loss ratios after 48 h of CO_2/$SCCO_2$ saturation in the pressure range 3 to 13 MPa. The larger permeability loss

Table 3
Modeling parameter magnitudes for numerical simulations on coal permeability.

Parameter	Value
Young's modulus of coal (E)	3.0 GPa
Poisson's ratio of coal (ν)	0.3
Biot coefficient (α)	0.8
CO_2 saturation pressure (P_f)	1–13 MPa
Confining stress (σ_1)	15 MPa
Initial reservoir pressure (P_{f0})	1.0 MPa
Initial matrix permeability (k_{mo})	$1.0 \times 10^{-19} m^2$
Langmuir pressure constant (P_L)	2.5 MPa
Langmuir strain constant (ε_L)	0.00159
Initial fracture permeability ratio (k_{fo}/k_{m0})	$100 - 1000$
Elastic modulus reduction ratio (R_m)	0.2–0.3
Sorption amplifier factor (f_s)	$9 - 14$

ratio represents strong continuous adsorption after the first 6-h saturation. In the subcritical region, the permeability loss ratio first increases as pressure increases from 3 to 5 MPa, and then decreases after the peak. This behavior can be explained in terms of Langmuir isothermal adsorption, where the adsorption reaches its maximum capacity at high pressures and thus only slightly adsorbs CO_2 in the high pressure range. The sorption-induced swelling causes a reduction in pore space and closure of the cleat system - decreasing permeability.

When the CO_2 becomes supercritical, the permeability loss ratio again increases at 7.5 MPa and then gradually declines. It can be inferred that the coal has a renewed susceptibility to swelling due to CO_2 adsorption after the critical pressure, resulting in an increase in the permeability loss ratio. The largest permeability losses are 70% and 74% at 5 MPa and 7.5 MPa for subcritical and supercritical CO_2, respectively. The smallest pressure losses are 26% and 43% for the two regions, occurring at 3 MPa and 13 MPa. The abrupt change at 7.5 MPa correlates to the permeability reduction that occurs immediately after the critical pressure, indicating that CO_2 adsorption may be increased. In summary, the influence of saturation time on permeability loss decreases as pressure increases, but the supercritical state of CO_2 causes more permeability loss after the phase transition.

The evolution of permeability to CO_2 with pore pressure for different saturation times is shown in Fig. 6. CO_2 permeability continues to
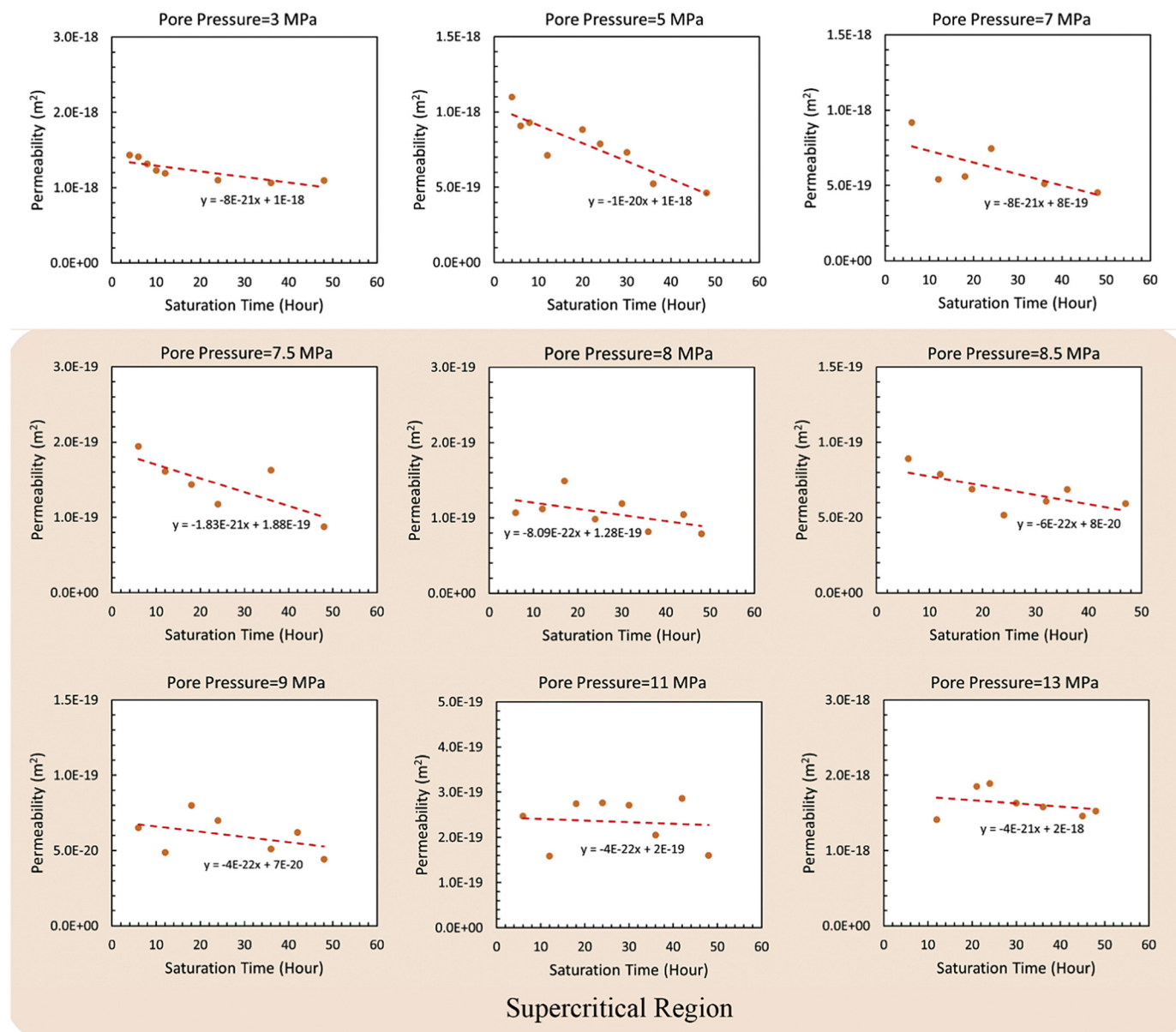

Fig. 4. Evolution of permeability with increasing saturation time at different pore pressures for the bituminous coal (T1504-CO_2).
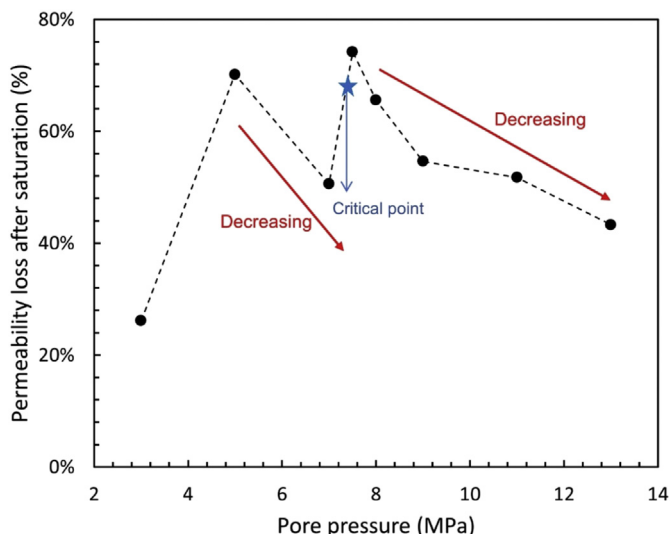
Fig. 5. Summary of permeability loss ratios after 48-h $CO_2/SCCO_2$ saturation for pressures in the range 3 to 13 MPa. A smaller permeability loss ratio means that permeability is relatively less time-dependent. The influence of saturation time on permeability loss decreases was pressure increases with the supercritical state inducing a renewed permeability loss after the phase transition.
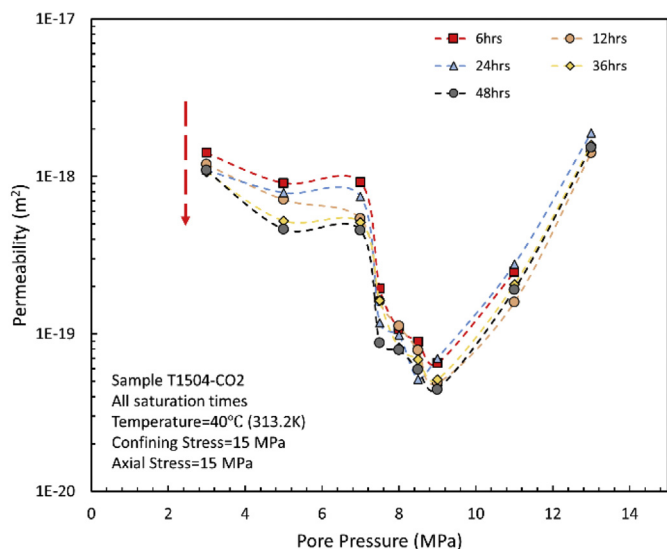

Fig. 6. CO_2 permeability evolution versus pore pressure at saturation times of 6, 12, 18, 24, 36 and 48 h at constant confining stress (15 MPa) and variable effective stress.

decrease with increased saturation time over the entire pressure range. Saturation time has a relatively larger influence at low pressures ($\leq$ 7.5 MPa) congruent with previous observations in $SCCO_2$ adsorption experiments (Perera et al., 2011). The intertwining of the permeability curves likely results from experimental uncertainty, especially for the ongoing adsorption during the 6-h measurement interval, corresponding to the scatted data in Fig. 4.

3.3. He and N_2 permeability

In this section, three distinctly different permeability profiles for coal saturated by different fluids are discussed. Fig. 7 shows the permeability comparison between $CO_2/SCCO_2$, Helium and Nitrogen under the same conditions, indicating that the types of saturating fluids have a significant impact on permeability evolution. Permeability increases monotonically as the saturation pressure of non-sorptive Helium
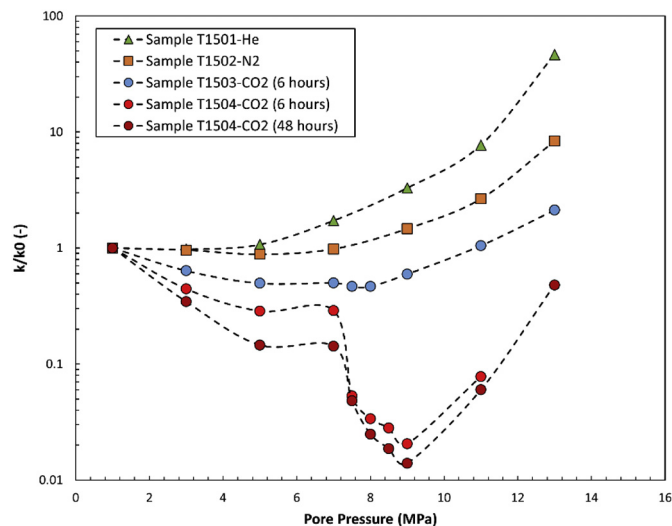

Fig. 7. Ensemble results for permeability ratio versus pore pressure for non-, slightly- and strongly-sorbing fluids.

increases due to the increase in effective stresses dilating cleats and fractures. The slightly-sorptive N_2 permeability ratio generally increases with an increase in saturation pressure, while at low pressures there is a slight permeability decrease indicating the minimal impact of sorption-induced swelling. A permeability reduction is generally observed at low pressures when adsorbable gases are present. This is because the sorption-induced matrix swelling results in a decrease in pore diameter and fracture aperture. As pore pressure increases the impact of effective stress further dominates over sorption-induced swelling. This switch in dominant behaviors causes the permeability to increase after the minimum permeability observed in the U-shaped permeability profile for N_2, CH_4 and CO_2 adsorptive gases. In this study, a measurable permeability reduction is observed for both N_2 and subcritical CO_2. For cases of T1503 and T1504, the CO_2 permeability rebounds after the saturation pressure of 5 MPa (e.g. Peng et al., 2014; Robertson and Christiansen, 2007).

When CO_2 pore pressure increases beyond the critical point, a second permeability reduction occurs. This reduction indicates that additional $SCCO_2$ adsorption occurs after the critical pressure. After reaching the minimum, $SCCO_2$ permeability again increases as pore pressure increases, leading to the W-shaped permeability evolution curve. In summary, the monotonically decreasing then increasing U-shaped, and W-shaped permeability profiles are for sub-critical-only fluids and for super-critical fluids undergoing the supercritical phase transition.

3.4. Impact of gas saturation on strength and deformability

Following the permeability tests, tri-axial strength experiments were conducted for the four specimens under 1.5 MPa confinement and 1.0 MPa pore pressure. All the tested samples were saturated at 13 MPa pressure of either He, N_2, or $CO_2/SCCO_2$ before the compression tests. The changes in coal mechanical properties are discussed by comparing tri-axial strength, Young's modulus and stiffness.

Fig. 8. shows the axial stress versus strain behavior after being saturated by the different fluids. Sample T1502-N_2 and T1501-He have the two largest tri-axial strengths, which are 27.29 and 22.93 MPa, respectively. When subjected to $SCCO_2$ adsorption, the tri-axial response decreased to 15.50 and 13.75 MPa for T1503 and T1504, respectively. Considering that T1501 is not influenced by sorption, strongly sorptive gas saturation results in a significant weakening by up to 43%. This is because the swelling stress induced by differential matrix swelling generates micro-cleats inside the saturated sample
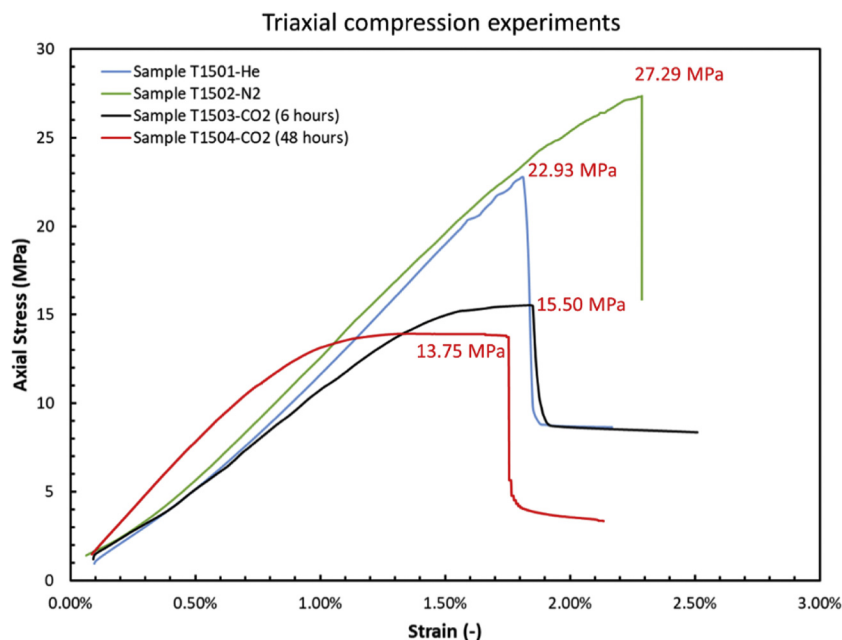
Fig. 8. Axial stress versus strain for bituminous coal following saturation by He, N_2 and $CO_2/SCCO_2$.

(Perera et al., 2011; Zhang et al., 2017). During saturation, these micro-cleats are discretely distributed and close due to sorption-induced swelling. After releasing the sorbing gas, prior to the compression tests, these discrete micro-cleats may play a significant role in generating a continuous macro-cleat or even a throughgoing fracture. Moreover, according to Griffith's criterion, the crack initiation stress threshold in a solid body is lowered due to the decrease in surface energy induced by exchanging a higher chemical potential adsorbate to the existing one (Gibbs, 1921; Griffith, 1921; Viete and Ranjith, 2006). The observed results are consistent with a decreasing trend in uniaxial compression strength (UCS) following CO_2 saturation, where the associated UCS reductions of 10% occur on exposure to gaseous CO_2 on lignite samples saturated at 3 MPa (Viete and Ranjith, 2006). The $CO_2/SCCO_2$ comparison experiment showed a 53% reduction in UCS for bituminous coal after CO_2 saturation at 6 MPa, while up to 78% reduction occurrs after $SCCO_2$ saturation to 12 MPa (Perera et al., 2013). The reported results show that supercritical CO_2 greatly reduces coal strength compared with gaseous CO_2 and other non-sorbing gases saturation. In addition, sample T1504 has a 140-fold smaller initial permeability that was supposed to have a higher mass strength, but it showed a weaker strength after 48-h $SCCO_2$ saturation at 13 MPa compared to T1503 with 6-h of $SCCO_2$ saturation at 13 MPa. It can be inferred that longer saturation time causes a larger reduction in tri-axial strength of coal.

The Young's moduli of coal samples after He, N_2, or $SCCO_2$ saturation are calculated from the slopes of the strain-stress relationships of Fig. 10. Considering that sample T1501-He has a similar initial permeability to T1503-CO_2, the difference between them can be regarded as due to the influence of CO_2 adsorption. After 6-h $SCCO_2$ saturation at 13 MPa, a 19.7% reduction in Young's modulus (E) occurs compared to Helium saturation, where E is ~1.37 GPa. Prior studies comparing Young's moduli between subcritical and supercritical CO_2 saturation show a sudden reduction in E when pore pressure changes from 6 MPa to 8 MPa, crossing the critical pressure (Perera et al., 2013). All these observations show that CO_2 saturation beyond the supercritical pressure has an increased potential to soften the coal structure, leading to a smaller modulus. This is because $SCCO_2$ coal plasticization causes re-arrangement in the physical structure of the coal and adds molecular mobility.

In this study, samples T1502 and T1504 have relatively higher E since they are transected by fewer natural fractures. Although T1504,

saturated by $SCCO_2$ at 13 MPa and for 48-h has the highest Young's modulus, its elastic strain is merely 0.8% at the onset of shear failure. After such a small elastic deformation, the slope decreases dramatically with the sample becoming plastic and failing rapidly. The elastic state for the other samples persists over a greater range of strains where the maximum elastic strain is 2.3% in the case of N_2.

Coal stiffness (units of kN/mm) is introduced to depict the alteration in mechanical structure due to the elastic-plastic transition in the tri-axial loading process. Stiffness here is obtained from the ratio between loading force and axial deformation. Fig. 9 shows the change in coal stiffness with increasing axial strain for the four samples. For the first three samples, coal stiffness first increases and then gradually decreases as the loading stress increases. The early-stage increment in stiffness is due to the elastic compaction of coal mass with the subsequent decrease
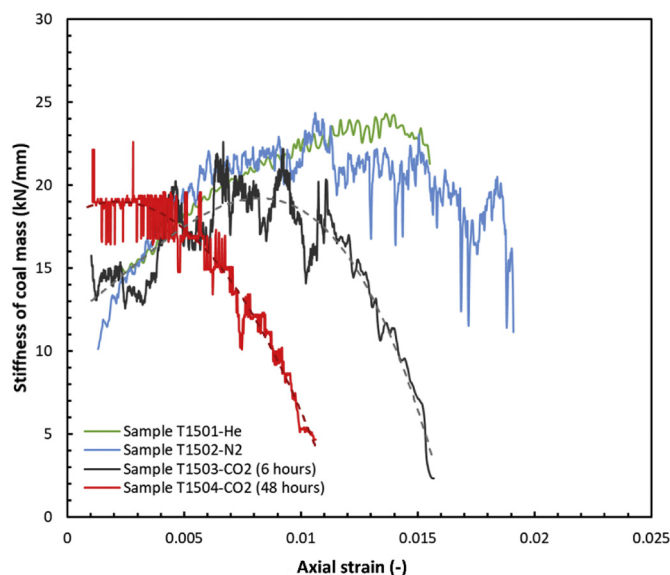

Fig. 9. Coal stiffness changes during tri-axial loading for the samples after He, N_2 and $CO_2/SCCO_2$ saturation. $SCCO_2$ saturation has a significant influence in reducing coal stiffness, transiting the elastic deformation of the coal rapidly to plastic.
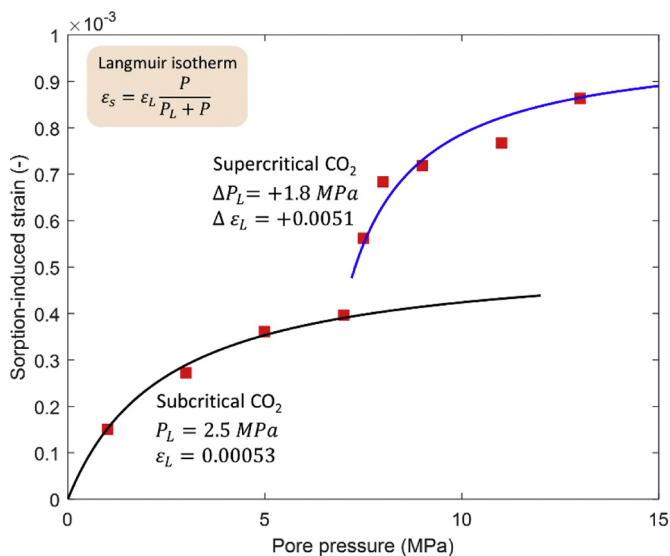
Fig. 10. The measured sorption-induced strain for sample T1504. Two Langmuir isotherms are introduced to fit the increment beyond the critical point in the experimental data.

Fig. 12. CO_2 density changes with increasing fluid pressure for different phases. The red arrows indicate the sharp increase in CO_2 density at the phase transition. Data adapted from McBride-Wright et al., 2015. (For interpretation of the references to colour in this figure legend, the reader is referred to the web version of this article.)

in stiffness representing irrecoverable plastic deformation. For T1501-He and T1502-N_2, the samples have a higher peak stiffness and the elevated stiffness is maintained around the peak until large deformations. But for the $SCCO_2$ saturated coal samples, after reaching its smaller peak value, the stiffness quickly declines, and the resultant plastic deformation results in rapid failure. Especially for sample T1504, after 48-h of $SCCO_2$ saturation, there is a marginal increment in stiffness but stiffness monotonically decreases soon after the beginning of loading. Clearly, $SCCO_2$ saturation has a significant influence in reducing coal stiffness, rapidly transitioning the elastic deformation to plastic.
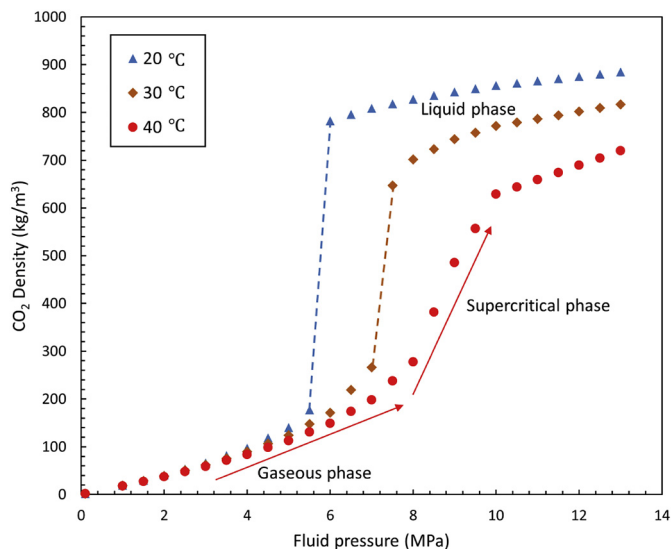
4. Discussion

In this section, the principal mechanisms behind the observed W-shaped permeability evolution with CO_2 phase transition are explored. The changes in coal compressibility and $SCCO_2$ adsorption capacity are attributed as the main causative factors for the permeability reduction above the critical pressure. The W-shaped pressure-permeability profile is the result of the competition between the dilative/permeability-increase influence of reduced effective stress and the enhanced CO_2/$SCCO_2$ adsorption at increasing gas pressure.
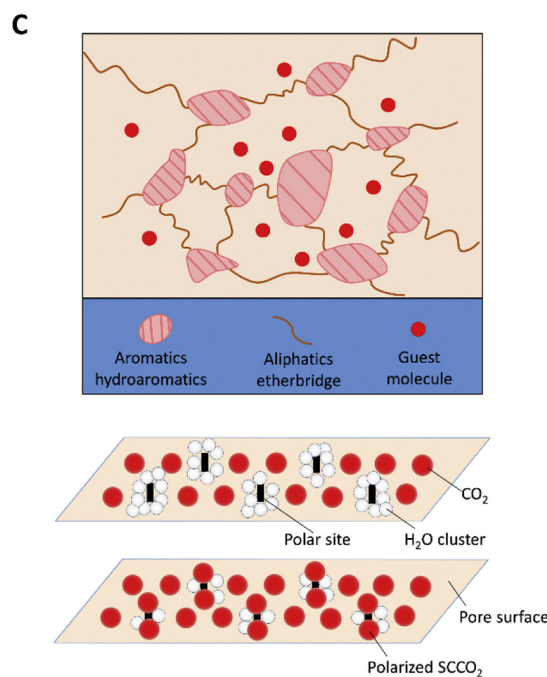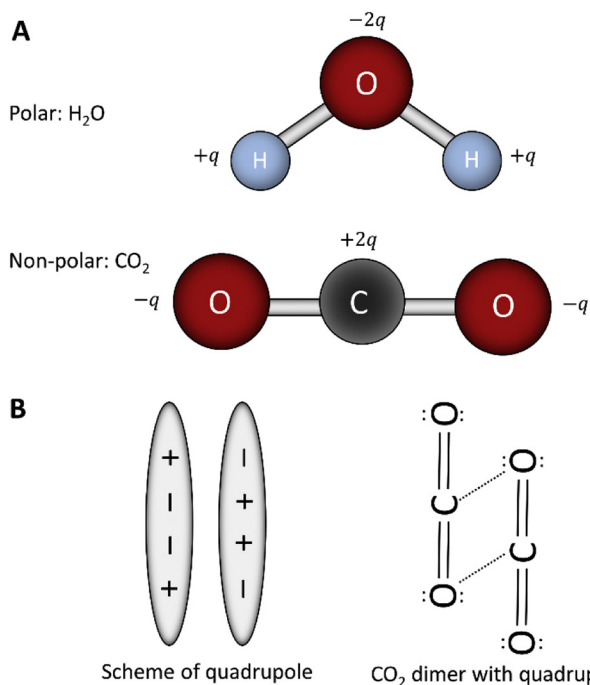

Fig. 11. (A) Molecular structure of H_2O and CO_2; (B) Proposed structure of CO_2 dimer with quadrupole moment; (C) Scheme of $SCCO_2$ adsorbed on polar sites. Adapted from Day et al., 2008 and Van Heek, 2000.
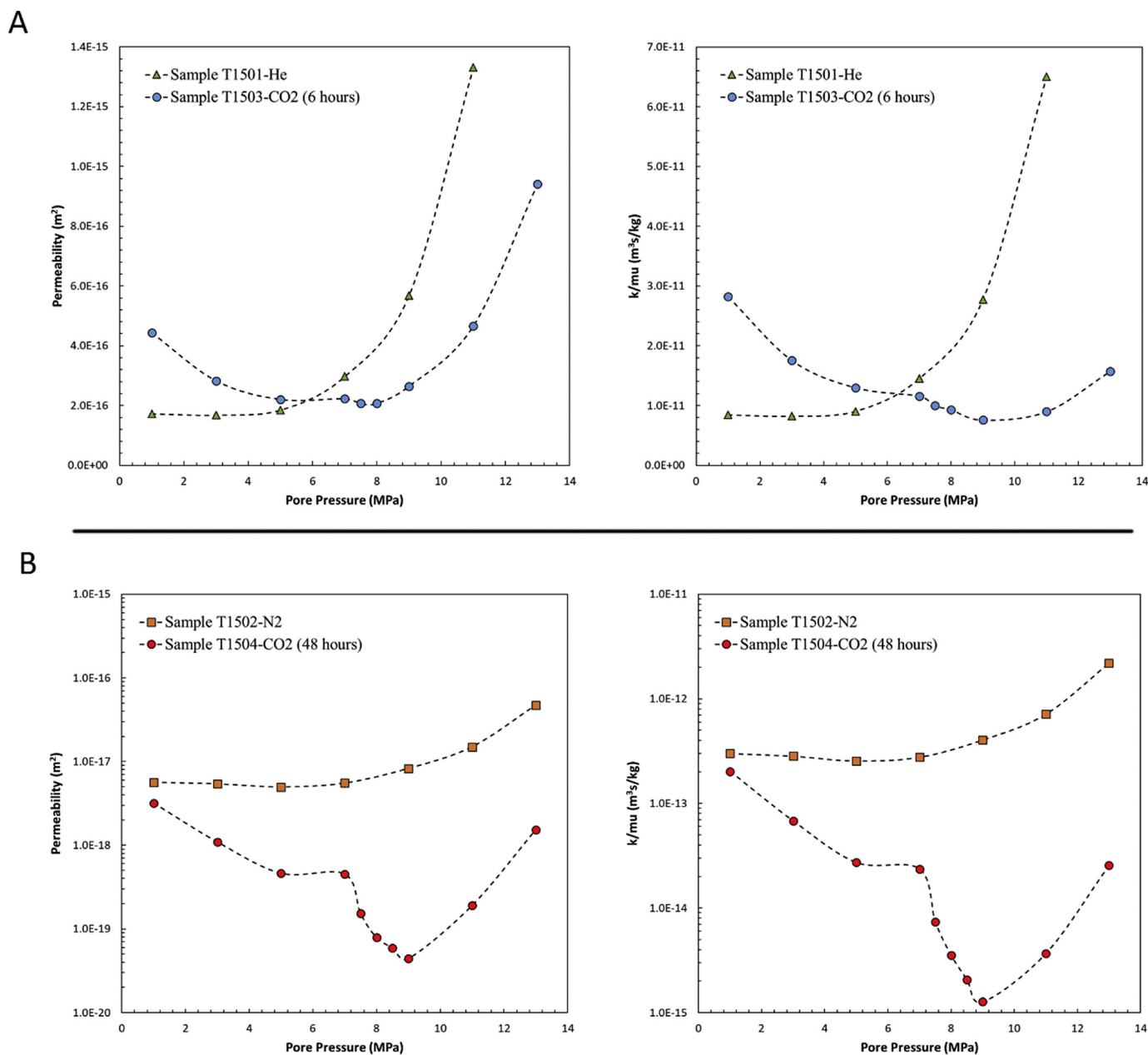
Fig. 13. Evolution of absolute permeability versus pore pressure and permeability over dynamic viscosity of the saturated fluids for the four samples. (A) Sample T1501-He and T1503-CO$_2$; (B) Sample T1502-N$_2$ and T1504-CO$_2$.

4.1. Plasticizing effect of SCCO$_2$

The effect of SCCO$_2$ adsorption on coal mechanical properties can be explained by the plasticization effect. Coal can be conceptualized as a glassy, porous, cross-lined polymeric macromolecular system. For a glassy solid, the intramolecular interaction energy is greater than the available thermal energy so the molecules and molecular segments lack the freedom to move except for small-scale rotations and vibrations (Larsen, 2004). Coal becomes rubbery when it interacts with a solvent or is warmed to a temperature such that the thermal energy is greater than the intramolecular interaction energy (Mirzaeian et al., 2006). For a rubbery material, its shape is retained due to the cross-linked structure, but now large-scale molecular motion is possible.

When injected into coal, CO$_2$ acts as a plasticizer enabling re-arrangements in the coal physical structure, adding molecular mobility, and converting coals from glass to rubbery. It has been extensively observed in both this study and the literature that CO$_2$ adsorption

weakens coal. When CO$_2$ is changed from a subcritical to supercritical state, the weakening effect on the coal mechanical properties becomes more significant since SCCO$_2$ is a stronger plasticizer. SCCO$_2$ has a stronger interaction with the active sites on the pore surface compared to subcritical CO$_2$. Moreover, SCCO$_2$ can further lower the glass transition temperature T$_g$ and facilitate coal to become even more rubbery at lower temperatures. Both the observations in this study and in previously published experiments (Masoudian et al., 2014; Perera et al., 2011b; White et al., 2005) have confirmed that the plasticization caused by SCCO$_2$ saturation softens the coal during saturation and consequently has a strong weakening effect in coal strength and stiffness. When saturation pressure increases, the induced reduction in the compression modulus results in renewed mechanical compression and cleat closures under in-situ stress condition. Therefore, the rubbery-like mechanical properties of coal contribute to the permeability decrease above the SCCO$_2$ phase change. Although it has been reported that the micro-cleats are generated by the internal swelling stress, this
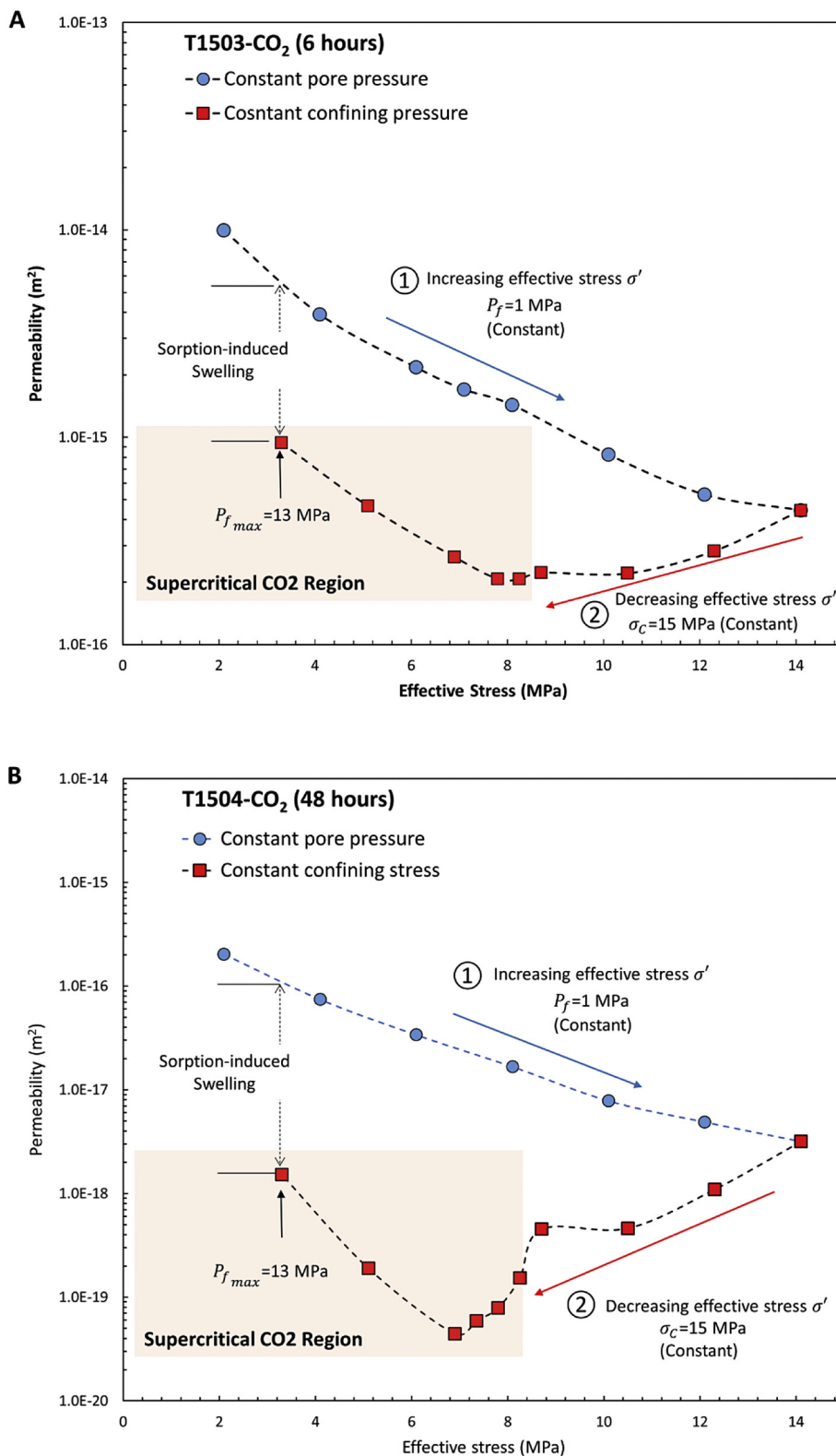
Fig. 14. Evolution of coal permeability with confining stress and pore pressure across the CO_2/$SCCO_2$ transition. Clear hysteresis is observed for the loading and unloading paths of effective stress. (A) For sample T1503-CO_2; (B) For sample T1504-CO_2.

microstructural fracturing exerts little influence on coal permeability since the fractures are closed and discretely distributed (Zhang et al., 2017).

4.2. Increased SCCO₂ sorption capacity

Fig. 11 shows that a sudden increment in the sorption-induced strain occurs after the critical pressure (T1504). The Langmuir constants used in the Langmuir adsorption model to match the

experimental data are listed in the plot. At a pore pressure of 13 MPa, the measured swelling strain is 93% greater than the Langmuir model predicts. To fit the excess sorption-induced swelling at pressures above 7.4 MPa, a secondary Langmuir isotherm is introduced with P_L of 1.8 MPa and $\varepsilon_L = 0.0051$ indexed relative to the critical point. The porous medium dilates when its surface energy changes, as a result of adsorption (Pan and Connell, 2007). When the surface of the pore space binds with the adsorbate, a reduction in specific surface energy ($\Delta\gamma > 0$) occurs. This reduction in surface energy is equal to the elastic strain energy that causes dilation of the matrix ($\varepsilon_r < 0$), expressed by Eq. 6 (Scherer, 1986).

$$\varepsilon_r = \frac{P}{3K_s} = -2\Delta\gamma/3rK_s \tag{6}$$

where ε_r is the e radial strain of the pore space, r is the radius of sphere experiencing a hydrostatic stress P and K_s is the bulk modulus.

Therefore, the measured increment in adsorption-induced strain is a result of the enlarged CO_2 adsorption capacity in the supercritical state. A similar result has been reported that an abrupt increase in the adsorbed amount of CO_2 occurs above the critical pressure (Toribio et al., 2005).

One important reason for the enlarged adsorption capacity is that the $SCCO_2$ molecules are more attracted to the adsorption sites on the pore surface. CO_2 is normally treated as non-polar because the symmetrical disposition of two oxygen atoms double-bonded to the carbon in its molecular structure, shown in Fig. 11(A). The hydrophobic sites on coal remain available for adsorption of nonpolar molecules, like CO_2 and CH_4 (Day et al., 2008). Meanwhile, the polar sites, such as hydroxyl groups, are preferentially occupied by water clusters on the pore surface since water is polar. However, it has been suggested that the rather polar nature of $SCCO_2$ results from the electrostatic interactions between the large quadrupole moment of $SCCO_2$ and the pore surface (Blatchford et al., 2003; Kauffman, 2001; Melikova, 2002; Raveendran et al., 2002; Raveendran et al., 2003). Fig. 11(B) and (C) show the structure of the CO_2 dimer with quadrupole and the adsorption competition between $SCCO_2$ and H_2O molecules on polar sites, respectively. The pore surface preferentially replaces the existing adsorbate with more reactive molecules to reduce surface energy (Mukherjee and Misra, 2018). This competition leads to more $SCCO_2$ adsorption aided by the quadrupole-dipole interactions.

Another fundamental change in the $SCCO_2$ fluid properties related to its transition is its increased density. When CO_2 becomes supercritical, it can flow and expand like gas but with a density like that of a liquid. Fig. 12 shows that CO_2 density changes with variable pressure at different temperatures. When the temperature is lower than the critical temperature ~31 °C, gaseous CO_2 suddenly becomes liquid and a significant increase in density occurs as the fluid pressure increases. If the temperature is above the critical temperature, $SCCO_2$ density within the vicinity of the critical pressure gradually increases with a relatively smaller slope compared to the case at low temperatures. But it still increases rapidly with respect to density in the lower pressure region, as shown by the red arrows. Compared to CO_2 at 1 MPa, CO_2 density is increased 11-fold and 36-fold at 7 and 10 MPa, respectively. The nearl-liquid density intensifies the interactions between the pore surface and the $SCCO_2$ molecules, causing more $SCCO_2$ molecules to be packed on the adsorbing layer for the same pore surface area. It is also argued that the high-density molecules can be more easily attracted to polar sites, like carboxyl functional group, resulting in an increase in CO_2 adsorption (Geng et al., 2009; Liu and Wilcox, 2012; Gensterblum et al., 2014b).

4.3. Effect of CO_2 viscosity

Above the critical point, CO_2 viscosity increases together with density. Although it is reported that $SCCO_2$ viscosity is gas-like, its viscosity is still greater than that of gaseous fluids. At 40 °C, CO_2

dynamic viscosity is increased ~4-fold as pressure increases from 1 to 13 MPa, while N_2 dynamic viscosity merely increases by 14% (Nordbotten et al., 2005). For Darcy flow in a porous medium, CO_2 permeability decreases as its dynamic viscosity increases. It is worth investigating the effect of dynamic viscosity change on the permeability evolution above the critical point. Fig. 13 shows the evolution in absolute permeability versus pore pressure for the four samples. The ratio of fluid permeability to dynamic viscosity is shown next to its absolute permeability to investigate whether the W-shaped permeability is the result of the increased $SCCO_2$ viscosity. The results indicate that the increased $SCCO_2$ viscosity has only a marginal effect in shaping the $SCCO_2$ permeability profile. Therefore, changes in $SCCO_2$ adsorption capacity and coal mechanical compressibility, rather than the increased fluid viscosity, principally contribute to the permeability reduction observed above the critical pressure.

Coal permeability, especially fracture permeability, will be significantly reduced as a result of the increased sorption-induced swelling. This is the main causative factor for the sudden permeability drop at the phase transition.

4.4. Effective stress response

As a poroelastic response, permeability reduction results from increasing effective stress, as a function of confinement and pore pressure. The impact of effective stress on permeability is reversible. However, it is clear that the experimental results are not consistent with this assumption for the CO_2 adsorption case. Fig. 14 shows how permeability evolves at variable effective stress under the two different stress conditions. The Biot coefficient here is assumed as 0.9 based on experimental measurements. Coal permeability decreases at a constant pore pressure of 1 MPa as the confining stress increases from 3 to 15 MPa, equal to effective stresses of 2.1 to 14.1 MPa. During this loading process, the permeability decrease is only determined by the increment in mechanical effective stress. The result shows that coal permeability decreases logarithmically as depth increases. Permeability increases at a constant confining stress of 15 MPa as the pore pressure increases from 1 to 13 MPa, equal to an effective stress of 14.1 to 3.3 MPa. The supercritical permeability region is highlighted by an orange box.

A large permeability gap exists between these two processes (Fig. 14), showing a clear hysteresis for the loading and unloading paths in effective stress. The permeability difference in the hysteresis represents the permeability reduction due only to the $CO_2/SCCO_2$ transition under confinement. Meanwhile, the reduced effective stress due to the increasing pore pressure results in dilation and cleat opening, especially when the coal is softened by CO_2 plasticization. The W-shaped pressure-permeability profile is the result of the competition between the increased effective stress effect and the response to $CO_2/SCCO_2$ adsorption. In summary, there are four processes impacting CO_2 permeability evolution and associated with the phase transition: (1) Permeability first decreases due to CO_2 adsorption-induced swelling as saturation pressure increases, even as the effective stress decreases during this process; (2) As the saturation pressure continues to increase (before the critical point), the permeability begins to increase as the impact of CO_2 adsorption is overcome by the reduced effective stress; (3) An abrupt permeability drop appears within the vicinity of the critical pressure as a result of the CO_2 phase transition; (4) After the second permeability reduction, $SCCO_2$ permeability again increases as $SCCO_2$ saturation pressure increases and the corresponding effective stress decreases.

It is worth noting that the resultant permeability at 13 MPa pore pressure is a maximum even though the sorption-induced permeability reduction (the gap in the hysteresis) is also a maximum for sample T1503. This is because the impact of decreasing effective stress is dominant when pore pressure is close to the confining stress. A similar trend is also shown in the case of T1504 but with a smaller absolute

permeability reduction because of its smaller initial permeability. The narrow fractures and small pores are more sensitive to the decrease induced by the CO_2 sorption. It is recognized that large injection pressure close to the in situ confining stress benefits CO_2 transport due to a large absolute permeability. To limit fluid migration in CO_2 sequestration, the pore pressure should be retained where the minimum permeability occurs above the critical pressure.

5. Conclusions

The evolution of coal permeability is measured in response to saturation by Helium, Nitrogen, CO_2/ $SCCO_2$ under variable effective stresses and pore pressures at a constant temperature of 40 °C. Tri-axial strength is measured, post-test, to investigate the influence of fluid saturation on the mechanical properties of deformability and strength – and thereby on permeabilty. A previously un-reported W-shaped permeability evolution is observed under CO_2/$SCCO_2$ saturation instead of the typical U-shaped permeability evolution. Three distinctly different forms of permeability evolution are illustrated by the non-sorbing (He), slightly-sorbing (N_2) and strongly sorbing (CO_2) fluids. Sorption-induced changes in the fluid and mechanical properties are analyzed to define mechanisms controlling the permeability profiles. The following conclusions can be drawn:

1. The influence of saturation time in reducing permeability generally decreases with an increase in the saturation pressure due to isothermal Langmuir adsorption. However, transition to the super-critical state for CO_2 causes a greater permeability loss after the phase transition, where coal permeability also becomes more time-dependent than before the critical pressure at the $SCCO_2$ transition.

2. The experiments contrasting the response for the non-, slightly- and strongly-sorbing gases define four processes contributing to the W-shaped CO_2 permeability evolution with phase transition. These are: (1) Permeability first decreases due to CO_2 adsorption-induced swelling as saturation pressure increases, even as effective stress decreases during this process; (2) As the saturation pressure continues to increase (before the critical point), the permeability begins to increase as the impact of CO_2 adsorption is overcome by the reduced effective stress; (3) An abrupt permeability drop appears within the vicinity of the critical pressure as a result of the CO_2 phase transition; (4) After the second permeability reduction, $SCCO_2$ permeability again increases as the pressure increases and the corresponding effective stress decreases.

3. Measurement of permeability to non-sorbing Helium (He) and slightly-sorbing Nitrogen (N_2) contrast the three distinctly different permeability evolution modes. Contrasting U-shaped and W-shaped permeability profiles are identified for slightly/strongly-sorptive fluids and strongly-sorptive fluids with phase transition, respectively.

4. $SCCO_2$ acts as a strong plasticizer enabling rearrangement of the physical structure and adding molecular mobility. Reduction in deformation modulus is also observed in the $SCCO_2$ saturated samples. The softened coal responds to increased compressional deformation and cleat closure under the same effective stress, resulting in an increase in permeability reduction in the supercritical region.

5. The permeability reduction observed above the critical pressure is also attributed to the increased adsorption capacity to $SCCO_2$. At a pore pressure of 13 MPa, the measured swelling strain is 93% more than the Langmuir model predicts. To fit the additional swelling strain, an extra Langmuir isotherm may be introduced with a P_L of 1.8 MPa and ε_L of 0.0051 indexed relative to the critical point. The enlarged $SCCO_2$ adsorption capacity presumably results from the slightly polar nature of the $SCCO_2$ dimer and the increased $SCCO_2$ density. The increase in $SCCO_2$ viscosity is shown to only marginally affect the form of the $SCCO_2$ permeability profile.

6. Apparent from the hysteresis in permeability, the CO_2/$SCCO_2$

adsorption-induced permeability reduction always increases with a decrease in effective stress under constant confinement. The $SCCO_2$ permeability at a pore pressure of 13-MPa is a maximum even though the sorption-induced permeability reduction is also maximum. It is recognized that large injection pressure close to the in situ confining stress benefits CO_2 transport due to a large absolute permeability. To limit fluid migration in CO_2 sequestration, the pore pressure should be retained where the minimum permeability occurs above the critical pressure.

7. Comparing coal samples with distinctly different initial permeabilities, heterogeneity (initial fracture spacing) is shown to play a controlling role in the permeability reduction, especially within the vicinity of the critical transition pressure.

References

Blatchford, M.A., Raveendran, P., Wallen, S.L., Hill, C., Carolina, N., 2003. Spectroscopic Studies of Model Carbonyl Compounds in CO 2 : Evidence for Cooperative C - HO Interactions. pp. 10311–10323. https://doi.org/10.1021/jp027208m.

Day, S., Sakurovs, R., Weir, S., 2008. Supercritical Gas Sorption on Moist Coals. 74. pp. 203–214. https://doi.org/10.1016/j.coal.2008.01.003.

Fujioka, M., Yamaguchi, S., Nako, M., 2010. CO_2 -ECBM field tests in the Ishikari Coal Basin of Japan. Int. J. Coal Geol. 82 (3–4), 287–298. https://doi.org/10.1016/j.coal.2010.01.004.

Geng, W., Nakajima, T., Takanashi, H., Ohki, A., 2009. Analysis of carboxyl group in coal and coal aromaticity by Fourier transform infrared (FT-IR) spectrometry. Fuel 88 (1), 139–144. https://doi.org/10.1016/j.fuel.2008.07.027.

Gensterblum, Y., Busch, A., Krooss, B.M., 2014a. Molecular concept and experimental evidence of competitive adsorption of H_2O, CO_2 and CH_4 on organic material. Fuel 115, 581–588. https://doi.org/10.1016/j.fuel.2013.07.014.

Gensterblum, Y., Ghanizadeh, A., Krooss, B.M., 2014b. Gas permeability measurements on Australian subbituminous coals: fluid dynamic and poroelastic aspects. J. Nat. Gas Sci. Eng. 19, 202–214. https://doi.org/10.1016/j.jngse.2014.04.016.

Gibbs, J.W., 1921. On the equilibrium of heterogeneous substances. In: The Collected Works of J. Willard Gibbs. vol. 1. pp. 55–353.

Griffith, A.A., 1921. The phenomena of rupture and flow in solid. By. Philos. Trans. R. Soc. Lond. 221 (587), 163–198.

Izadi, G., Wang, S., Elsworth, D., Liu, J., Wu, Y., Pone, D., 2011. Permeability evolution of fluid-infiltrated coal containing discrete fractures. Int. J. Coal Geol. 85, 202–211. https://doi.org/10.1016/j.coal.2010.10.006.

Jones, S.C., 1997. A Technique for Faster PulseĆDecay Permeability Measurements in Tight Rocks, (December 1996). pp. 25–28.

Kauffman, J.F., 2001. Quadrupolar solvent effects on solvation and reactivity of solutes dissolved in supercritical CO_2. J. Phys. Chem. 105 (14). https://doi.org/10.1021/jp004359l.

Kumar, H., Elsworth, D., Mathews, J.P., Marone, C., 2015. Permeability evolution in sorbing media : analogies between organic-rich shale and coal. Geofluids. https://doi.org/10.1111/gfl.12135.

Lal, R., 2008. Sequestration of atmospheric CO_2 in global carbon pools. Energy Environ. Sci. https://doi.org/10.1039/b809492f.

Larsen, J.W., 2004. The Effects of Dissolved CO_2 on Coal Structure and Properties. 57. pp. 63–70. https://doi.org/10.1016/j.coal.2003.08.001.

Liu, Y., Wilcox, J., 2012. Molecular Simulation Studies of CO_2 Adsorption by Carbon Model Compounds for Carbon Capture and Sequestration Applications.

Liu, J., Chen, Z., Elsworth, D., Miao, X., Mao, X., 2011. Evolution of coal permeability from stress-controlled to displacement-controlled swelling conditions. Fuel 90 (10), 2987–2997. https://doi.org/10.1016/j.fuel.2011.04.032.

Liu, T., Lin, B., Yang, W., 2017. Impact of matrix – fracture interactions on coal permeability: model development and analysis. Fuel 207, 522–532. https://doi.org/10.1016/j.fuel.2017.06.125.

Masoudian, M.S., Airey, D.W., El-Zein, A., 2014. Experimental investigations on the effect of CO_2 on mechanics of coal. Int. J. Coal Geol. 128–129, 12–23. https://doi.org/10.1016/j.coal.2014.04.001.

Massarotto, P., Golding, S.D., Bae, J., Iyer, R., Rudolph, V., 2010. Changes in reservoir properties from injection of supercritical CO_2 into coal seams — a laboratory study. Int. J. Coal Geol. 82 (3–4), 269–279. https://doi.org/10.1016/j.coal.2009.11.002.

Mavor, M.J., Corp, T., Gunter, W.D., Robinson, J.R., 2004. Alberta Multiwell Micro-Pilot Testing for CBM Properties, Enhanced Methane Recovery and CO 2 Storage Potential. SPE, (January 2004). pp. 1–15.

Mcbride-wright, M., Maitland, C., Trusler, J.P.M., 2015. Viscosity and density of aqueous solutions of carbon dioxide at temperatures from (274 to 449) K and at pressures up to 100 MPa. J. Chem. Eng. https://doi.org/10.1021/je5009125.

Melikova, S.M., 2002. Unusual Spectroscopic Properties of CF_3H Dissolved in Liquified

Ar, N$_2$, CO, and CO$_2$. 352. pp. 301–310 January.

Mirzaeian, M., Hall, P.J., Kingdom, U., 2006. The Interactions of Coal with CO$_2$ and its Effects on Coal Structure. vol. 8. pp. 2022–2027.

Mukherjee, M., Misra, S., 2018. A review of experimental research on Enhanced Coal Bed methane (ECBM) recovery via CO$_2$ sequestration. Earth Sci. Rev. 179 (June 2017), 392–410. https://doi.org/10.1016/j.earscirev.2018.02.018.

Nordbotten, J.A.N.M., Celia, M.A., Bachu, S., 2005. Injection and storage of CO$_2$ in deep saline aquifers: analytical solution for CO$_2$ plume evolution during injection. Transp. Porous Med. 339–360. https://doi.org/10.1007/s11242-004-0670-9.

Pan, Z., Connell, L.D., 2007. A Theoretical Model for Gas Adsorption-Induced Coal Swelling. pp. 243–252. https://doi.org/10.1016/j.coal.2006.04.006.

Peng, Y., Liu, J., Wei, M., Pan, Z., Connell, L.D., 2014. Why coal permeability changes under free swellings : New insights. Int. J. Coal Geol. 133, 35–46. https://doi.org/10.1016/j.coal.2014.08.011.

Peng, Y., Liu, J., Pan, Z., Connell, L.D., Chen, Z., Qu, H., 2017. Impact of coal matrix strains on the evolution of permeability. Fuel 189, 270–283. https://doi.org/10.1016/j.fuel.2016.10.086.

Perera, M.S.A., Ranjith, P.G., Choi, S.K., Airey, D., 2011a. The effects of sub-critical and super-critical carbon dioxide adsorption-induced coal matrix swelling on the permeability of naturally fractured black coal. Energy 36 (11), 6442–6450. https://doi.org/10.1016/j.energy.2011.09.023.

Perera, M.S.A., Ranjith, P.G., Peter, M., 2011b. Effects of saturation medium and pressure on strength parameters of Latrobe Valley brown coal : Carbon dioxide, water and nitrogen saturations. Energy 36 (12), 6941–6947. https://doi.org/10.1016/j.energy.2011.09.026.

Perera, M.S.A., Ranjith, P.G., Viete, D.R., 2013. Effects of gaseous and super-critical carbon dioxide saturation on the mechanical properties of bituminous coal from the Southern Sydney Basin. Appl. Energy 110, 73–81. https://doi.org/10.1016/j.apenergy.2013.03.069.

Ranathunga, A.S., Perera, M.S.A., Ranjith, P.G., Bui, H., 2016. Super-critical CO$_2$ saturation-induced mechanical property alterations in low rank coal: an experimental study. J. Supercrit. Fluids 109, 134–140. https://doi.org/10.1016/j.supflu.2015.11.010.

Raveendran, P., Wallen, S.L., Uni, T., Carolina, N., Hill, C., Carolina, N., 2002. Cooperative CHO Hydrogen Bonding in CO$_2$ - Lewis Base Complexes : Implications for Solvation in Supercritical CO$_2$. vol. 15. pp. 12590–12599. https://doi.org/10.1021/ja0174635.

Raveendran, P., Wallen, S.L., Hill, C., Carolina, N., 2003. Exploring CO$_2$ –Philicity: Effects of Stepwise Fluorination. pp. 1473–1477. https://doi.org/10.1021/jp027026s.

Robertson, E., Christiansen, R., 2007. Modeling laboratory permeability in coal using sorption-induced-strain data. SPE Reserv. Eval. Eng. 10 (3), 9–12. https://doi.org/10.2118/97068-PA.

Scherer, G.W., 1986. Dilatation of Porous Glass. vol. 80. pp. 473–480.

Seidle, J.R., Huitt, L.G., 1995. Experimental measurement of coal matrix shrinkage due to gas desorption and implications for cleat permeability increases. Int. Meeting Petrol. Eng. https://doi.org/10.2118/30010-MS.

Syed, A., Durucan, S., Shi, J., Korre, A., 2013. Flue gas injection for CO$_2$ storage and enhanced coalbed methane recovery: mixed gas sorption and swelling characteristics of coals. Energy Procedia 37, 6738–6745. https://doi.org/10.1016/j.egypro.2013.06.607.

Toribio, M.M., Oshima, Y., Shimada, S., 2005. Coal adsorption capacity measurements using carbon dioxide at sub-critical and supercritical conditions. In: Greenhouse Gas Control Technologies II.

Van Bergen, F., Damen, K., Gale, J., Lysen, E., 2005. Identification of Early Opportunities for CO$_2$ Sequestration — Worldwide Screening for CO$_2$ -EOR and CO 2 -ECBM Projects. vol. 30. pp. 1931–1952. https://doi.org/10.1016/j.energy.2004.10.002.

Van Heek, K.H., 2000. Progress of coal science in the 20th century. Fuel 79, 1–26.

Viete, D.R., Ranjith, P.G., 2006. The effect of CO$_2$ on the geomechanical and permeability behaviour of brown coal : Implications for coal seam CO$_2$ sequestration. Int. J. Coal Geol. 66, 204–216. https://doi.org/10.1016/j.coal.2005.09.002.

Vishal, V., 2016. In-situ disposal of CO$_2$: liquid and supercritical CO$_2$ permeability in coal at multiple down-hole stress conditions. J. CO$_2$ Utiliz. 17, 235–242. https://doi.org/10.1016/j.jcou.2016.12.011.

Wang, S., Elsworth, D., Liu, J., 2011. Permeability evolution in fractured coal: the roles of fracture geometry and water-content. Int. J. Coal Geol. 87 (1), 13–25. https://doi.org/10.1016/j.coal.2011.04.009.

Wang, S., Elsworth, D., Liu, J., 2013. Permeability evolution during progressive deformation of intact coal and implications for instability in underground coal seams. Int. J. Rock Mech. Min. Sci. 58, 34–45. https://doi.org/10.1016/j.ijrmms.2012.09.005.

Wang, Y., Liu, S., Elsworth, D., 2015. Laboratory investigations of gas fl ow behaviors in tight anthracite and evaluation of different pulse-decay methods on permeability estimation. Int. J. Coal Geol. 149, 118–128. https://doi.org/10.1016/j.coal.2015.07.009.

Wang, G., Wang, K., Wang, S., Elsworth, D., Jiang, Y., 2018. An improved permeability evolution model and its application in fractured sorbing media. J. Nat. Gas Sci. Eng. 56 (January), 222–232. https://doi.org/10.1016/j.jngse.2018.05.038.

White, C.M., Smith, D.H., Jones, K.L., Goodman, A.L., Jikich, S.A., Lacount, R.B., ... Schroeder, K.T., 2005. Sequestration of carbon dioxide in coal with enhanced coalbed methane recovery s A Review†. J. Nat. Gas Sci. Eng. 19 (3). https://doi.org/10.1021/ef040047w.

Wu, Y., Liu, J., Elsworth, D., Chen, Z., Connell, L., Pan, Z., 2010. Dual poroelastic response of a coal seam to CO$_2$ injection. Int. J. Greenhouse Gas Control 4 (4), 668–678. https://doi.org/10.1016/j.ijggc.2010.02.004.

Wu, Y., Liu, J., Chen, Z., Elsworth, D., Pone, D., 2011. A dual poroelastic model for CO$_2$-enhanced coalbed methane recovery. Int. J. Coal Geol. 86, 177–189. https://doi.org/10.1016/j.coal.2011.01.004.

Zhang, J., Liang, Y., Pandey, R., Harpalani, S., 2015. Characterizing microbial communities dedicated for conversion of coal to methane in situ and ex situ. Int. J. Coal Geol. 146, 145–154. https://doi.org/10.1016/j.coal.2015.05.001.

Zhang, Y., Lebedev, M., Sarmadivaleh, M., Barifcani, A., Iglauer, S., 2016. Swelling-induced changes in coal microstructure due to supercritical CO$_2$ injection. Geophys. Res. Lett. 9077–9083. https://doi.org/10.1002/2016GL070654.Received.

Zhang, Y., Zhang, Z., Sarmadivaleh, M., Lebedev, M., Barifcani, A., 2017. Micro-scale fracturing mechanisms in coal induced by adsorption of supercritical CO$_2$. Int. J. Coal Geol. 175 (February), 40–50. https://doi.org/10.1016/j.coal.2017.04.002.

Zhang, S., Liu, J., Wei, M., Elsworth, D., 2018. Coal permeability maps under the in fluence of multiple coupled processes. Int. J. Coal Geol. 187 (January), 71–82. https://doi.org/10.1016/j.coal.2018.01.005.

Zhi, S., Elsworth, D., 2016. The role of gas desorption on gas outbursts in underground mining of coal. Geomech. Geophys. Geo-Energy Geo-Resources 2 (3), 151–171. https://doi.org/10.1007/s40948-016-0026-2.

Zhi, S., Elsworth, D., Wang, J., Gan, Q., Liu, S., 2018. Hydraulic fracturing for improved nutrient delivery in microbially-enhanced coalbed-methane (MECBM) production. J. Nat. Gas Sci. Eng. 60 (August), 294–311. https://doi.org/10.1016/j.jngse.2018.10.012.